

Evaluating the opposing wave interaction hypothesis for the generation of microbaroms in the eastern North Pacific

Kristoffer T. Walker¹

Received 31 July 2012; revised 15 October 2012; accepted 19 October 2012; published 13 December 2012.

[1] Two microphone arrays were deployed in California during 2010 to record microbaroms, quasi-continuous atmospheric pressure oscillations with a period of ~ 5 s. In this paper a time-progressive, frequency domain beamforming method is developed and used to analyze microbaroms recorded by these and 10 other infrasonic arrays along the North Pacific rim. Common pelagic microbarom sources that move around the North Pacific are observed during the boreal winter. Summertime North Pacific sources are only observed by western Pacific arrays, presumably a result of weaker microbarom radiation and westward stratospheric winds. A well-defined source is resolved ~ 2000 km off the coast of California in January 2011 that moves closer to land over several days. The source locations are corrected for deflection by horizontal winds using acoustic ray trace modeling with range-dependent atmospheric specifications provided by ground-to-space models. The observed source locations do not correlate with anomalies in NOAA Wave Watch 3 (NWW3) model field data. However, application of the opposing wave, microbarom source model of Waxler and Gilbert (2006) to the NWW3 directional wave height spectra output at buoy locations within 1100 km of the western North America coastline predicts microbarom radiation in locations that correlate with observed locations. These results suggest that pelagic North Pacific microbarom radiation detected by infrasonic arrays during the boreal winter could be routinely used to validate NWW3 results in regions with poor sensor coverage.

Citation: Walker, K. T. (2012), Evaluating the opposing wave interaction hypothesis for the generation of microbaroms in the eastern North Pacific, *J. Geophys. Res.*, 117, C12016, doi:10.1029/2012JC008409.

1. Introduction

[2] Oscillations called “microseisms” and “microbaroms” that are associated with spectral peaks at periods from 2 to 20 s are one of the most recognizable sources of background noise in recordings of surface displacement and atmospheric infrasound, respectively [Wiechert, 1904; Benioff and Gutenberg, 1939]. Microseisms, microbaroms, and ocean wave activity have often been correlated, and the dominant microseism and microbarom periods are often half the associated ocean wave period [e.g., Bernard, 1937; Deacon, 1947; Darbyshire, 1962]. Microseismic radiation usually occurs in three different areas: deep ocean basins [e.g., Iyer, 1958; Haubrich and McCamy, 1969; Bromirski et al., 2005], near shorelines [e.g., Baird and Banwell, 1940; Haubrich et al., 1963; Cessaro, 1994; Tabulevich, 1995; Friedrich et al., 1998; Bromirski, 2001; Gerstoft et al., 2006; Gerstoft

and Tanimoto, 2007], and near or beneath atmospheric depressions [e.g., Ramirez, 1940; Gilmore, 1946; Donn and Naini, 1973; Haubrich and McCamy, 1969; Zhang et al., 2010]. These studies show that microseisms are observable in seismic Rayleigh, Love, and P waves. The development of larger and denser networks of stations like the USArray Transportable Array or Japanese Hi-net are improving our ability to locate microseism sources [e.g., Zhang et al., 2010].

[3] There have been relatively far fewer studies of microbaroms than microseisms. Gutenberg and Benioff [1941] showed that microbaroms and microseisms have the greatest amplitudes in the boreal winter months in southern California. They also found a correlation between these phenomena and depressions off the coast. Donn and Posmentier [1967] and Donn and Naini [1973] found correlations between the location of elevated wave heights due to atmospheric depressions in the North Atlantic and the projection of microbarom detection back azimuths recorded by an array in New York. They attributed the microbaroms due to the interference of opposing waves in the vicinity of the elevated wave heights.

[4] The adoption of the Comprehensive Nuclear Test Ban Treaty (CTBT) in 1996 led to the development of the International Monitoring System (IMS), which will include a 60-station, global network of infrasonic arrays with apertures ranging from 1 to 3 km [Christie and Campus, 2010].

¹Institute of Geophysics and Planetary Physics, Scripps Institution of Oceanography, University of California, San Diego, La Jolla, California, USA.

Corresponding author: K. T. Walker, Institute of Geophysics and Planetary Physics, Scripps Institution of Oceanography, University of California, San Diego, 9500 Gilman Dr., La Jolla, CA 92093-0225, USA. (kwalker@ucsd.edu)



Figure 1. Photos of a CHIAR array element. Each OFIS sensor was 30 m long and covered by a bear-resistant wire cage. Power at each element was provided by three 12 V batteries charged by two 200 W solar panels. Data was wirelessly transmitted to UCSD in real time via 900 MHz radios.

Although the IMS network is still under construction, 45 infrasonic arrays are currently recording data.

[5] The University of California, San Diego (UCSD) recently installed two infrasonic arrays in California to improve the station coverage for the purposes of locating coastal sources of microbaroms. The first array was installed between Los Angeles and San Diego at the Santa Margarita Ecological Reserve (SMIAR), 30 km from the coast. Nine microbarometers were distributed over an aperture of 700 m to minimize the possibility of spatial aliasing of monochromatic infrasound in the 0.2 to 1 Hz band. Four 15 m long porous hoses were connected to each microbarometer for wind noise reduction. A second array was installed in northern California near the city of Chico (CHIAR; Figure 1). This array comprises four optical fiber infrasound sensors (OFIS) in a centered triangle configuration with an aperture of 925 m. OFIS sensors are line microphones that instantaneously average pressure along their lengths with laser interferometry [Zumberge *et al.*, 2003]. Although the sensor has a very low noise floor, the benefit of the sensor over other technologies is its effectiveness at reducing wind noise without degrading the measured infrasonic signal of interest, which cannot be achieved using pipe rosettes [Walker and Hedlin, 2010].

[6] Since the adoption of the CTBT, infrasonic arrays have provided new insights into processes that impact the solid earth, oceanographic, and atmospheric science communities [e.g., Hedlin *et al.*, 2012]. For example, it has been hypothesized for decades that stratospheric wind controls most infrasonic propagation through the effective sound speed, which is the sum of the static sound speed (mostly a function of temperature) and the component of wind in the direction of propagation. Because the static sound speed at the Earth's surface is often approximately the same as that in the stratosphere, the horizontal stratospheric wind can form ground-to-stratospheric ducts for propagation in downwind directions. Le Pichon *et al.* [2004] showed that this was true

by highlighting a correlation between the prevailing direction of the stratospheric winds and microbarom arrival azimuths observed by austral IMS arrays. Le Pichon *et al.* [2006] took that work further and showed that microbaroms are observed at several middle- and high-latitude IMS arrays. The arrival azimuths and amplitudes of the signals exhibit seasonal trends that correlate with the seasonal reversals of the stratospheric winds. They found that in the northern hemisphere, microbaroms are detected generally from sources east of the arrays during the boreal summer and west of the arrays during the winter. The trend is reversed in the southern hemisphere. A scaling relation between the signal amplitude and the strength of the upper wind further suggests that most of the microbarom energy propagates in ground-to-stratosphere ducts. Within the seasonal pattern, microbarom detections can be modulated by wind noise and more local and diurnal variations in atmospheric conditions [Kulichkov *et al.*, 2004]. In fact, the variation of microbaroms can be used to invert for upper atmospheric wind and temperature structure [e.g., Donn and Rind, 1971; Rind and Donn, 1975; Garces *et al.*, 2004; Le Pichon *et al.*, 2005; Drob *et al.*, 2010a], which is useful because current upper atmospheric wind models do not include global-scale planetary waves, interseasonal variability, and nonmigrating tides. More recently, Landes *et al.* [2012] analyzed several years of data recorded by the IMS arrays. They used a cross-bearings source location approach to show that the predominant global microbarom radiation is also affected by the location of the most turbulent seas, with dominant radiation around Greenland from September through April and around the South Pacific from May through August.

[7] This paper presents the analysis of infrasonic data recorded by twelve arrays along the rim of the North Pacific Ocean. It is shown that the microbarom radiation from common pelagic sources is often strong enough to overcome

inefficient propagation conditions and be detected simultaneously at most arrays during the boreal winter. Conversely, during the summer, only weaker North Pacific sources are detected by western Pacific arrays. A winter source in the eastern North Pacific that was recorded by five eastern Pacific arrays is analyzed in careful detail. It is shown that the observed microbarom radiation is consistent with that predicted by applying the *Waxler and Gilbert* [2006] hypothesis to directional wave height spectra output by NOAA Wave Watch 3 (NWW3) models at the locations of buoys that provided input data to these models. Specifically, the empirically estimated microbarom source location correlates with the location of an area of opposing ocean waves of the same ~ 10 s period. The paper is organized in the following manner. Section 2 explains the array processing method FTBeam used to detect and characterize the recorded infrasound. Section 3 describes the results of the data analyses. Section 4 details the modeling of the observations using output from NWW3. Finally, sections 5 and 6 discuss and summarize these results, respectively.

2. Frequency-Time Beamforming (FTBeam)

[8] Many techniques exist for detecting planar wave energy that crosses an array. An effective technique is the progressive multichannel correlation method (PMCC), which involves cross correlation of waveforms recorded by different sensor triplets [*Cansi*, 1995]. Another method called beamforming generates a beam function

$$B(\theta, V) = \sum_j^m \left(\sum_i^n a_i(t_j + t_i^p(\theta, v, r_x, r_y)) \right)^2 \quad (1)$$

where a_i is the i th receiver amplitude, n is the number of receivers, t_j is the j th time sample within a specified time window, m is the number of time samples in each window, t_i^p is the predicted time shift to align the waveforms at the reference point, r_x and r_y indicates the relative position of the receivers, and θ and V are the trial optimum parameters back azimuth and apparent phase speed across the array, respectively. The trial time shift is $t_i^p = \vec{r} \cdot \hat{k} / V$, where \hat{k} is the unit vector in the trial propagation direction across the array that depends on θ . This time shift can be applied in the time domain (as implied by equation (1)), but it is more useful to apply it in the frequency domain. The typical range of V for infrasound is 300 to 450 m/s. The maximum of $B(\theta, V)$ indicates a possible detection of infrasound at the associated arrival time, azimuth, and apparent phase velocity. Using this approach, a frequency-time beamforming program called FTBeam has been developed for the detection and characterization of coherent infrasound recorded by an array. The general method and important equations are described in the three steps below.

2.1. Step 1: Frequency-Domain Beamforming

[9] The first step comprises dividing the time series into windows with 66% overlap. Each window is detrended and Hanning tapered such that the amplitudes within the 33% overlap at both ends are greatly attenuated. Fourier transforms are then computed using the FFTW method [*Friego and Johnson*, 1999]. Frequency domain beamforming is performed for each frequency-time (FT) window over a trial

grid of (θ, V) that characterize planar wave propagation across the array [*DeMuth*, 1977]. The complex beams at the individual frequencies are then averaged across frequency bins (typically 10 per decade) for the trial grid of optimum parameters. The maximum value of the magnitude of the complex beam function across the grid determines the optimum parameters for each FT window or “pixel.”

2.2. Step 2: Detection and Family Classification

[10] The first step results in two-dimensional arrays of optimum θ , optimum V , and maximum beam power as a function of frequency and time. Step 2 is a detection algorithm that groups pixels together based on the evaluation across neighboring pixels of a Euclidean distance equation

$$d^2 = \left(\frac{\Delta t}{\sigma_t} \right)^2 + \left(\frac{\Delta f}{\sigma_f} \right)^2 + \left(\frac{\Delta \theta}{\sigma_\theta} \right)^2 + \left(\frac{\Delta V}{\sigma_V} \right)^2 \quad (2)$$

where Δt , Δf , $\Delta \theta$, and ΔV are the changes in time, frequency, back azimuth, and apparent phase velocity, and σ_t , σ_f , σ_θ , and σ_V are the family tuning parameters that determine the weights given to each grouping parameter, respectively. Equation (2) is a version of the original family clustering equation used in the PMCC algorithm [*Cansi*, 1995]. The power of this approach is that one can tune these parameters to detect coherent, long infrasonic wave trains buried in noise or short bursts of energy with high signal-to-noise ratios. If the number of clustered pixels is greater than a prescribed threshold, they are deemed “significant” pixels and define a family.

2.3. Step 3: Uncertainty Estimation

[11] The goal of the third step is to determine which families of pixels are significant and derive family signal parameters with statistically significant uncertainties. The ability of a time series to resolve model parameters is proportional to the time window length and frequency bandwidth; a long, narrow-band signal has the same model resolution power as a short, broadband signal. To account for this, a simple FT window is found that encloses 95% of the pixels for each family. Then a grid search is performed over trial parameters to minimize the sum of the square of the misfit $M(\theta, V)$ between all unique pairs of time-shifted waveforms. The global minimum determines the final optimum parameters that characterize the detection. M is used to obtain the 95% confidence region using the method of *Silver and Chan* [1991]. If one assumes that M may be regarded as χ_n^2 variable with n degrees of freedom, then one can construct the α confidence contour from

$$\frac{M(\theta, V)}{M_{\min}} \leq 1 + \frac{k}{n-k} f_{k, n-k}(1 - \alpha) \quad (3)$$

where k is the number of model parameters (2), and f is the inverse of the F probability distribution [*Jenkins and Watts*, 1968]. While this is true for Gaussian white noise ($n =$ number of time samples), it is not true for band-limited waveforms (coherent noise). To accommodate band-limited waveforms, the Silver and Chan approach assumes that M is approximately χ_n^2 distributed with

$$n = 2 \left(\frac{2E^2}{E_4} - 1 \right) \quad (4)$$

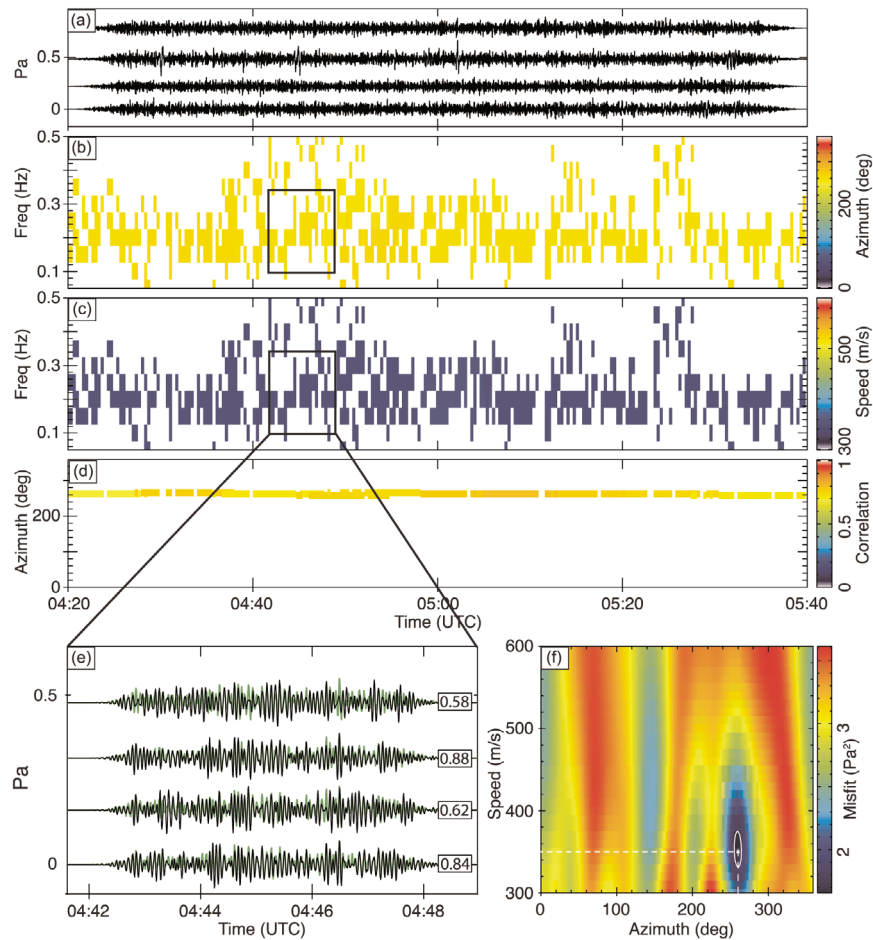


Figure 2. FTBeam results for IMS array IS56, located near Newport, Washington, during 29 January 2011. The x axis is the time since the start of the day. (a) The pressure time series in the 0.05 to 0.5 Hz passband. (b) The frequency of the pixels that have been assigned to families, with pixel color indicating the final family back azimuth. (c) The same as Figure 2b, except color now indicates the final family apparent speed. (d) The final family back azimuth as a function of time, with color indicating the family median correlation coefficient with respect to the optimum beams. (e) The optimally aligned waveforms compared with the associated optimum beam (green) for a particular family (enclosed in the box). The correlation coefficients between the beam and each trace are shown to the right. (f) The associated misfit grid with the 95% confidence region enclosing the optimum detection parameters.

where E and E_4 are the energy and fourth moment of the time series, respectively. The value of ν is usually much smaller than n and is independent of the sampling rate of the waveforms. For typical infrasound data, the ratio ν/n ranges from 0.1 to 0.3.

[12] Using this approach the 95% confidence region and asymmetric 2σ error bars for the optimum parameters are estimated via a grid search. Numerical experiments with adding white and band-limited noise to synthetic waveforms confirms that as the noise increases, the confidence region computed with this method expands to include the original model parameters. Furthermore, as the array aperture of signal frequency is modified in a way as to reduce its directional resolution power, the confidence region expands as expected. A final suite of quality control measures are based on the estimated uncertainties and the median of the correlation (in the time domain) of the optimum beam with the optimally time-shifted waveforms.

[13] An example of applying FTBeam on data from IMS array IS56 is shown in Figure 2. The coherent infrasound has a central frequency of 0.2 Hz and originates in this case from a source west-southwest of the array. The rather high average correlation coefficient and small 95% confidence region indicates that the detection is statistically significant.

3. Data Analysis Results

3.1. North Pacific Results

[14] Although the main study area of this paper is the eastern North Pacific, twelve IMS infrasonic arrays have been analyzed in the 0.05 to 0.5 Hz frequency band for all of 2011 around the Pacific rim to provide a basis for understanding the eastern North Pacific results. Starting near San Diego and moving counterclockwise around the North Pacific, these arrays are: SMIAR, IS57, NVIAR, CHIAR, IS56, IS53, IS44, IS45, IS30, IS39, IS24, and IS21. Most

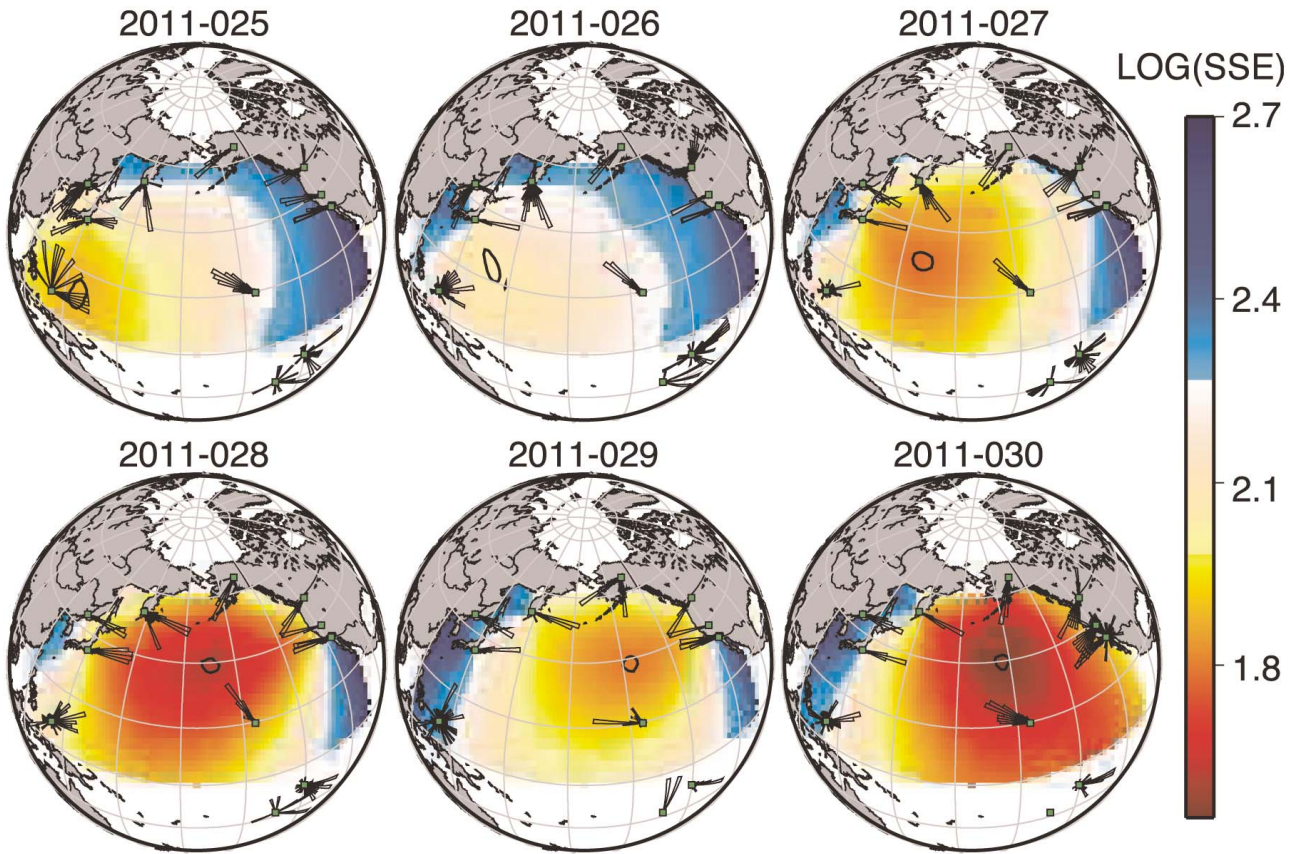


Figure 3. FTBeam results for the North Pacific showing a coherent source of microbarom radiation migrating from the western Pacific to the eastern Pacific over the course of 6 days (25–30 January 2011). Color is a proxy for the intersection density of projected back azimuths from each array (equation (5)). The 95% confidence region for a single source model is calculated using equation (3) and is shown in black.

2011 data were available from these arrays, but gaps in data availability (totaling >30% of the year) existed for CHIAR.

[15] Polar histograms showing the daily distribution of microbarom back azimuths have been normalized by the total number of detections for each array and are shown in Figure 3 for a 6 day period in January 2011. Correlations can be observed between many arrays that suggest a common source that moves coherently with time. To quantitatively show these correlations, the optimum source location for a common-source model is estimated by calculating

$$SSE(x, y) = \frac{1}{m} \sum_i^m \left(\frac{1}{n_i} \sum_j^{n_i} \left(\frac{\theta_{ij} - \theta_i^p(x, y)}{\sigma_{ij}} \right)^2 \right) \quad (5)$$

where θ_{ij} is the detected back azimuth; σ_{ij} is the asymmetric 2σ error bar; θ_i^p is the predicted back azimuth; i and j are the indices corresponding to the arrays m and number of array detections at each array n_i , respectively; and (x, y) are the spatial coordinates of grid points across the North Pacific. Equation (5) is a normalized sum of the square of the misfit between model predictions and observations. The 95% confidence region is calculated using equation (3). Implicit in this approach is the assumption that the source is a point source and that the spread of detection back azimuths for each array represents a measure of both the observed noise

level and the departure of the observations from a point source model. Consequently, the size of the confidence region could represent the influence of wind noise on array detections or a region of distributed microbarom radiation. The number of data degrees of freedom are set equal to the total number of detections, whereas the number of model parameters is set to $k = 2$. Detections from CHIAR are very similar to those from NVIAR and are not included in this computation to reduce the effect of east-west smearing of the source region from an asymmetric distribution of arrays.

[16] During this 6 day period, a single source is visible off the northeast coast of Palau that travels northeast to an area north of Hawaii. The 95% confidence interval is fairly large during the first 2 days when only a handful of arrays point to the same location. However, the 95% confidence region shrinks to a diameter of ~ 500 km during days 027–030 as more arrays are pointing to the same source region. Six days of IS99 microbarom detections made with PMCC (kindly provided by Milton Garces) are also represented by a polar histogram in Figure 3. These detections are not used in the evaluation of equation (5) because the detections were made using a different set of tuning parameters, the significance of the uncertainties provided by PMCC is not the same as that provided by FTBeam, and there is topographic blocking of infrasound by volcanoes on Hawaii for northeast and southeast back azimuths [Willis *et al.*, 2004]. Nonetheless,

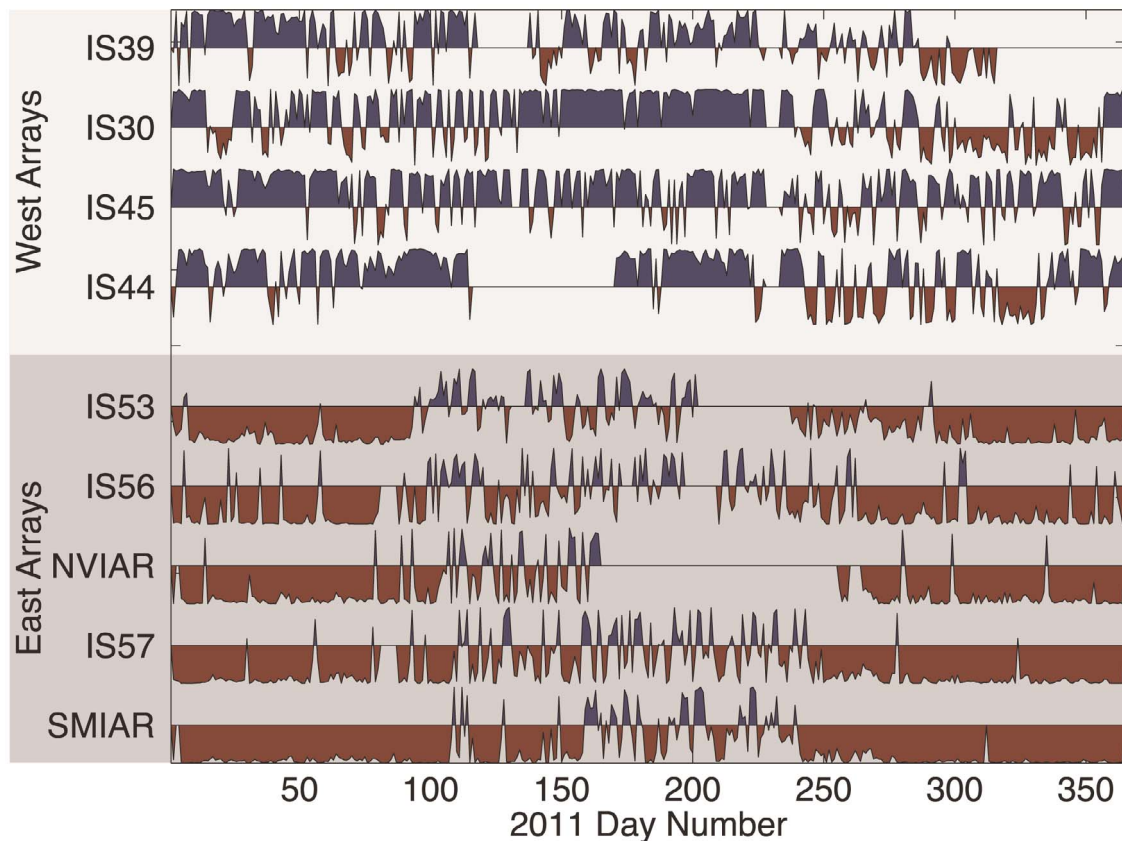


Figure 4. Histograms of the east-west component of the detection back azimuths for arrays to the east and west of the North Pacific for year 2011. Negative values (red) correspond to westerly back azimuths, while positive values (blue) correspond to detections from easterly back azimuths.

during this 6 day period, the IS59 back azimuths consistently rotate from a westerly direction toward the north during the first 4 days. On the fifth day (029), detections from due west begin to overpower the north-northwest detections. By the sixth day, the apparent source to the north of Hawaii is not visible to IS59.

[17] To better understand the entire year of data, the east-west component of the 2011 back azimuth detections are plotted for the eastern and western arrays (Figure 4). Gaps in available data coverage are shown as horizontal lines. During the boreal winter under eastward stratospheric wind conditions (September through mid-April), all arrays generally observe microbaroms from the North Pacific. However, during the summer when the stratospheric winds are reversed, microbaroms are detected from many different directions at the eastern arrays, while they are consistently detected from North Pacific sources at the western arrays. This suggests that an increase in microbarom source strength in the winter overcomes the more inefficient propagation of infrasound upwind to the western Pacific arrays.

3.2. Eastern North Pacific

3.2.1. Ray Trace Modeling

[18] A coherent microbarom source was detected in the east North Pacific by the temporary and permanent infrasonic arrays in the western U.S. states and Alaska in November 2010 (days 319–324). These arrays include

SMIAR, IS57, NVIAR, CHIAR, IS56, and IS53. NVIAR is operated by the Southern Methodist University.

[19] Within this source-receiver geometry, when the back azimuths from these western U.S. arrays point due west, there exists an ambiguity in the location of the source using cross-bearing methods: either a common source exists in the deep Pacific basin or a source local to each array exists close to the coast. Because of this limited sensitivity and the fact that infrasound is routinely deflected along the source-receiver plane due to horizontal wind, correcting for this wind deflection may be important. A three-dimensional acoustic ray trace modeling program called ART2D (K. T. Walker, Acoustic Ray Tracer, 2D, 2011, <http://sail.ucsd.edu/~walker/software/ART2D/art2d.html>) is used with atmospheric specifications of temperature and wind provided by global ground-to-space models [Drob *et al.*, 2010b] to define ray deflection corrections for infrasonic propagation from buoy 46059 (a reference point in the eastern North Pacific about 550 km off the California coast) to all the arrays.

[20] The ray tracing identified the existence of a stratospheric duct for propagation to these arrays for all 6 days, consistent with the eastward stratospheric winds that characterize wintertime propagation conditions at U.S. latitudes [Le Pichon *et al.*, 2009; Walker *et al.*, 2011]. There were occasionally well developed tropospheric ducts as well over both the ocean and land. Using the predicted back azimuth

deflection angles, the observed back azimuths at the arrays were corrected prior to being used for source location.

3.2.2. Microbarom Source Location

[21] Daily polar histograms of array back azimuths for signals in the 0.05 to 0.5 Hz range are shown in Figure 5a. The \log_{10} of the relative frequency is shown as a rose diagram for each station. The size of each rose diagram is normalized by the maximum bin at each station. Correlations can be observed between neighboring arrays along the western U.S. coast that suggest a common source in the eastern North Pacific. It should be noted that IS53 in Alaska exhibits a predominant back azimuth that points toward the eastern North Pacific on day 321, but not during the other 2 days (Figure 5). As is shown later, this is likely due to the source strength off the coast of British Columbia increasing to a maximum on day 321.

[22] To quantitatively estimate this source location with uncertainties, equation (5) and the associated 95% confidence region for a common-source model is computed using just the corrected back azimuths from all five western U.S. arrays: SMIAR, IS57, NVIAR, CHIAR, and IS56. The microbarom source region generally moves during days 320–322 toward the U.S. west coast (Figure 5a). The 95% confidence region has an average diameter of ~ 350 km. As will be seen later, the source continues to move closer during day 323 as the confidence region shrinks to 150 km across. It should be noted that the application of the back azimuth corrections, which varied slowly over several days by $\pm 5^\circ$, moved the source closer to the coast by ~ 150 km, which is not far given the scale of the study region.

4. Modeling Microbarom Radiation

4.1. Wave-Wave Interaction

[23] *Miche* [1944] and *Longuet-Higgins* [1950] (LH) developed the leading hypothesis for the generation of double-frequency microseism energy. When two intersecting antiparallel waves have the same periods, the average pressure does not exponentially decrease with depth because of a second-order, nonlinear pressure term. The significant pressure fluctuations at the seafloor couple into the solid Earth mostly as Rayleigh waves and compressional P waves. *Longuet-Higgins* [1950] also showed that resonance is likely to occur in some regions for special combinations of frequency and water depth, in addition to along coastlines when incoming waves interfere with reflected waves. Notable studies by *Haubrich et al.* [1963] and *Hasselmann* [1963] investigated the influence of nearshore microseism generation and concluded that the sources of the double-frequency microseisms were generated locally due to resonance and coastal reflection of waves generated by distant storms.

[24] *Hasselmann* [1963] also introduced an important integral that quantifies the standing wave productivity due to the “wave-wave interaction” that is responsible for the microseism generation. For computational purposes using NOAA Wave Watch 3 (NWW3) output, this integral is cast into a finite sum

$$\Psi_{ijk} = 2 \sum_1^{p/2} F_{ij\frac{1}{2}l} F_{ij\frac{1}{2}l+\frac{p}{2}} \Delta\theta^2 \quad (6)$$

where F_{ijkl} is the directional wave energy spectral density output by NWW3 in units of $\text{m}^2/(\text{Hz rad})$ at an (x_s, y_s) point on the ocean surface. The indices i, j, k, l , and corresponding dimension lengths, m, n, o , and p , refer to x_s, y_s , frequency, and wave direction, respectively. The variable $\Delta\theta$ is the wave direction sampling interval. In other words, the standing-wave productivity for a given frequency is the summation over all directions of the product of the energy densities of opposing waves with the same half frequency.

[25] *Kedar et al.* [2008] showed an agreement between observed and predicted microseism amplitudes obtained by applying the LH hypothesis to predicted directional wave spectra provided by NOAA/NCEP Wave Watch 3 (NWW3). They focused on an area off the coast of southern Greenland, where two prominent sets of opposing waves routinely collide in an area far from coastlines where wave reflections are thought to have a minimal impact on opposing wave interaction. They predicted that southward moving waves along the southeast side of Greenland were interfering with opposing waves and creating elevated levels of Ψ that explained elevated microseism levels recorded by nearby seismometers.

[26] *Ardhuin et al.* [2011] extended the *Kedar et al.* [2008] work by developing a version of NWW3 that includes coastal reflections. They found that on land within a few hundred kilometers of the coast, double-frequency microseisms are routinely generated locally by the interference of the incident and reflected waves, but that this source is routinely overpowered by a stronger source of microseisms generated in the deeper ocean between two opposing wave sets.

[27] The leading hypothesis to explain microbaroms is that they are generated by the same wave-wave interaction that generates microseisms. *Waxler and Gilbert* [2006] define the atmospheric microbarom “source strength spectrum squared” as a real function of frequency for an infinitely deep ocean without acoustic resonances as

$$D_{ijk} = \frac{4\rho_a^2 g^2 \pi^4 f_k^3}{c_a^2} \left(\frac{9g^2}{4\pi^2 c_a^2 f_k^2} + \frac{c_a^2}{c_w^2} \right) \Psi_{ijk} \quad (7)$$

where ρ_a and c_a are the density and speed of sound in the atmosphere just above the sea surface, and c_w is the speed of sound in water. The first term represents the pressure generated in the water by the motion of the sea surface that leaks into the atmosphere in the source region. This term comprises $\sim 80\%$ of the total microbarom pressure above the source area [*Brekhovskikh et al.*, 1973; *Waxler and Gilbert*, 2006]. The second term represents the remaining $\sim 20\%$ due to the direct compression of the air above the standing ocean waves. The units of D are Pa^2/Hz . Note that Ψ is the common factor in both the microseism and microbarom generation.

[28] The observed microbarom spectral density at some remote point on the Earth’s surface can be modeled as the summation of pressure disturbances generated by point sources within a given source area that have been convolved with a propagation function. Specifically, the spectral density is

$$P_r(x_r, y_r, f) = \iint D(x_s, y_s, f) Q(x_s, y_s, x_r, y_r) dx_s dy_s \quad (8)$$

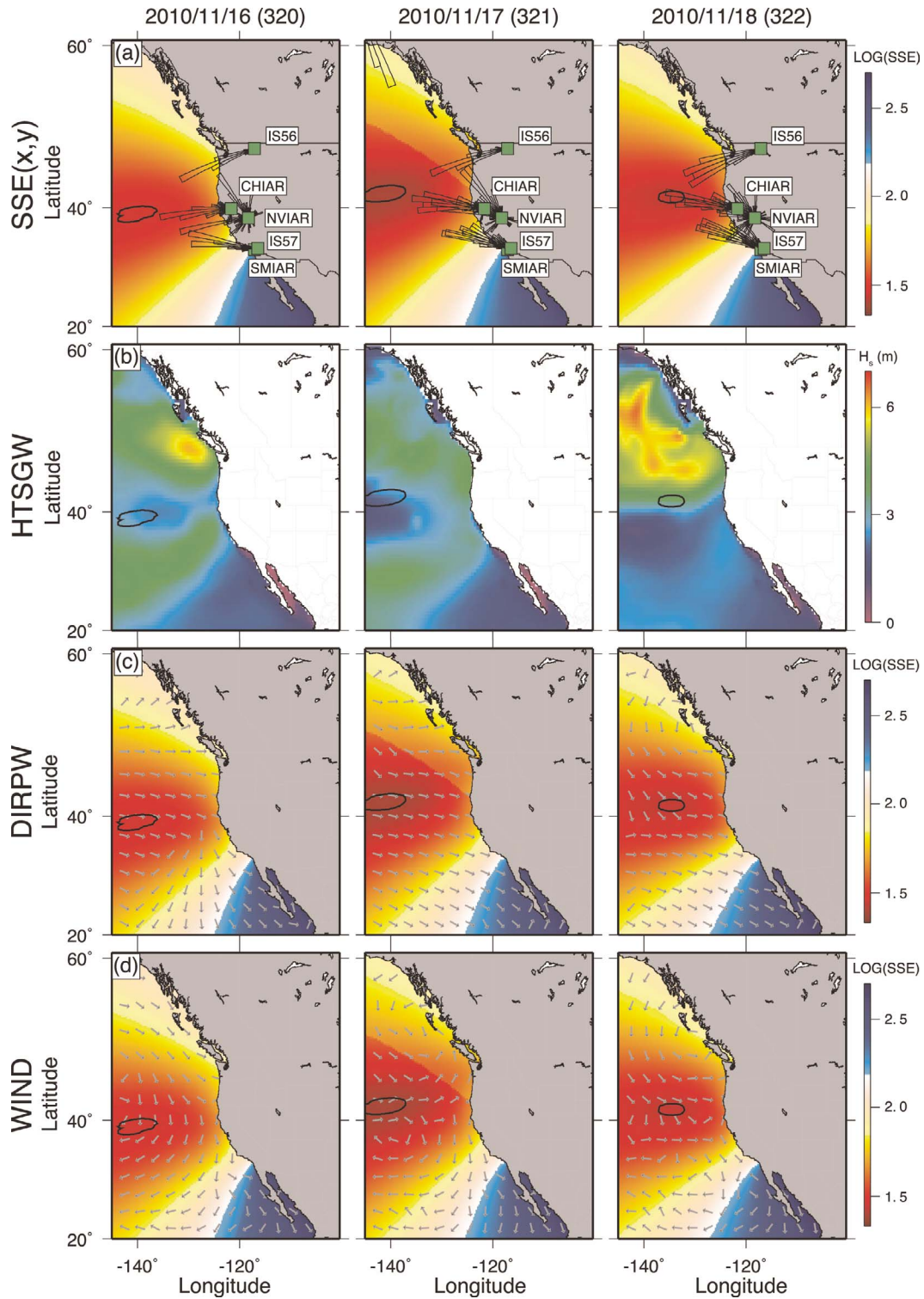


Figure 5. Comparison of observed microbaroms off the western U.S. coast to specifications provided by NOAA Wave Watch 3 2-D model fields. (a) Polar histograms of back azimuths centered at each station suggest a common source. Color is calculated using equation (5) and is a measure of the intersection density of the projected back azimuths. The black contour indicates the 95% confidence region. The 95% confidence region is compared with (b) the significant height of combined wind waves and swell (HTSGW), (c) the primary wave direction (DIRPW), (d) and the surface wind direction. The color map beneath the vectors in Figures 5c and 5d is the same as in Figure 5a.

where (x_r, y_r) are the coordinates of the receiver, and Q is the square of the magnitude of the Green's function, which has units of m^{-2} and is related to transmission loss by $TL = -10\log_{10}(Q)$ [Waxler and Gilbert, 2006]. For example, Stopa *et al.* [2011] multiplied D by the area A over which it was assumed to be in phase, assigned Q to 1 m^{-2} (ignoring propagation), and computed the peak microbarom pressure density above the ocean surface. Their focus was on the infrasound recorded by IMS array IS59 in Hawaii that was generated by Hurricane Felicia in 2009. They modeled the microbarom radiation of idealized depressions (without background wave activity) and predicted that the region of strong wave-wave interaction moves from the eye of a stationary depression to the wake of a moving depression. Array processing results from IS59 for Hurricane Felicia were in general agreement with the predicted trailing location of the opposing waves.

[29] Focusing on infrasonic recordings associated with a west Pacific typhoon recorded by an array on the island of Palau, Hetzer *et al.* [2008] showed a correlation between the observed infrasound and the location of opposing waves predicted by NOAA Wave Watch 3 (NWW3) model field data. IS39 microbarom back azimuths unambiguously pointed to the region where two predominant wave directions were opposing.

4.2. Comparing Eastern North Pacific Microbarom Radiation to 2-D Fields Directly From NWW3

[30] A test of the Waxler and Gilbert (WG) hypothesis with the eastern North Pacific observations would be to evaluate $D(x, y, f)$ using the directional wave spectra output by NWW3, as was done by Kedar *et al.* [2008] to test the LH hypothesis. However, this requires a detailed knowledge of how to operate NWW3. An alternative approach taken by many to date has been to use the publicly available NWW3 2-D field averages to compare microbarom or microseism source locations to regions of elevated significant wave height [e.g., Gerstoft *et al.*, 2008; Landes *et al.*, 2012], opposing dominant wave directions [Hetzer *et al.*, 2008], or opposing surface winds [Kedar *et al.*, 2008]. In general, the first approach using significant wave height assumes that as wave height increases, the total energy in the system increases, and therefore any opposing waves that exist in the system will give rise to stronger microbarom sources. The second and third approaches assume that within a region for any given time, the strongest microbaroms will be generated where there is a spatial transition in the dominance of one wave or wind set to another that is opposing in nature. All three of these approaches will give rise to correlations, but only when other conditions permit; lack of a correlation does not rule out microbarom generation.

[31] Focusing on the 3 days of microbarom detections during 16–18 November 2010, the 95% confidence region of the microbarom source is now compared to significant height of combined wind waves and swell (HTSGW; Figure 5b), direction of travel for the primary wave (DIRPW; Figure 5c), and the direction of travel for the surface winds used to run the hindcast NWW3 model registered on a $1^\circ \times 1^\circ$ grid (Figure 5d). The source region exhibits no correlation with HTSGW or DIRPW. There is a minor degree of correlation with the surface winds; the source region is only ~ 300 km northeast of an area of opposing

surface winds during day 321. However, there is no correlation on the other days. Furthermore, the estimated source region on day 321 is ~ 1000 km to the north-northwest of an area of opposing surface winds.

4.3. Comparing With the Waxler and Gilbert [2006] Model Using Directional Wave Spectra at Buoys

[32] The eastern North Pacific microbarom source does not correlate well with predictions from routine 2-D fields output by NWW3 (Figure 5). To provide a better evaluation of the Waxler and Gilbert [2006] hypothesis in explaining these observations, the directional wave spectra of hindcast NWW3 runs evaluated at the buoys that provided input data are now used to compute D_{ijk} . These directional spectra are routinely available on NOAA FTP sites. The peak microbarom pressure density source strength in dB (with reference to $1 \text{ Pa}^2/\text{Hz m}^2$) above the ocean is computed with

$$S_{MB}(x, y) = 10 \log_{10}(\max\{D(x, y, f = 0.15 : 0.25)\}Q) \quad (9)$$

As in Stopa *et al.* [2011], Q is assigned to 1 m^{-2} . Note that this definition of S_{MB} is different from that defined in Stopa *et al.* [2011] in that this definition is not proportional to an assumed source area size. Before computing equations (7) and (9), to validate the accuracy of the NWW3 hindcast results, raw wave height data and NWW3 directional spectra for buoy 46059 were integrated over direction and frequency to calculate significant wave heights, which were found to be within 3% of each other.

[33] The computation of S_{MB} is shown for days 319–324, spanning the time frame in Figure 5. The resulting values are linearly interpolated between the buoy locations using a Delaunay triangulation approach (Figure 6), which does not provide predictions farther than ~ 1100 km from the coast due to the limited buoy coverage. The generally slow variation in color across the eastern North Pacific suggests that predicted fine-scale variations between the buoys are relatively minor. Polar back azimuth histograms are shown for arrays SMIAR, CHIAR, IS56, and IS53; IS57 and NVIAR are not included because of higher wind noise levels in the deserts during days 323 and 324.

[34] The dynamic range of S_{MB} throughout the eastern North Pacific is ~ 100 dB, with the same -30 dB maximum occurring on days 323 and 324 (Figure 6). The -33 dB contour (white) is defined to illuminate the predicted source area more clearly. The empirically defined 95% confidence region (black contour) during days 319–321 is too far from the coast to be compared with buoy predictions. However, one can see that the predicted microbarom strength increases in the region that the confidence region migrates into during subsequent days. The maximum value of S_{MB} occurs on two days: 323 and 324. On day 323, the predicted microbarom strength is consistent and overlaps with the 95% confidence region. On day 321, there is a significant increase in predicted source strength just off the coast of northern British Columbia. The predicted level is almost above the -33 dB contour and is consistent with the IS53 microbarom observations. The discrepancy between the confidence region and predicted source area off the coast of California for day 324 is discussed later.

[35] Additional insight is gained by inspecting the NWW3 directional wave energy density spectrum at buoy 46059,

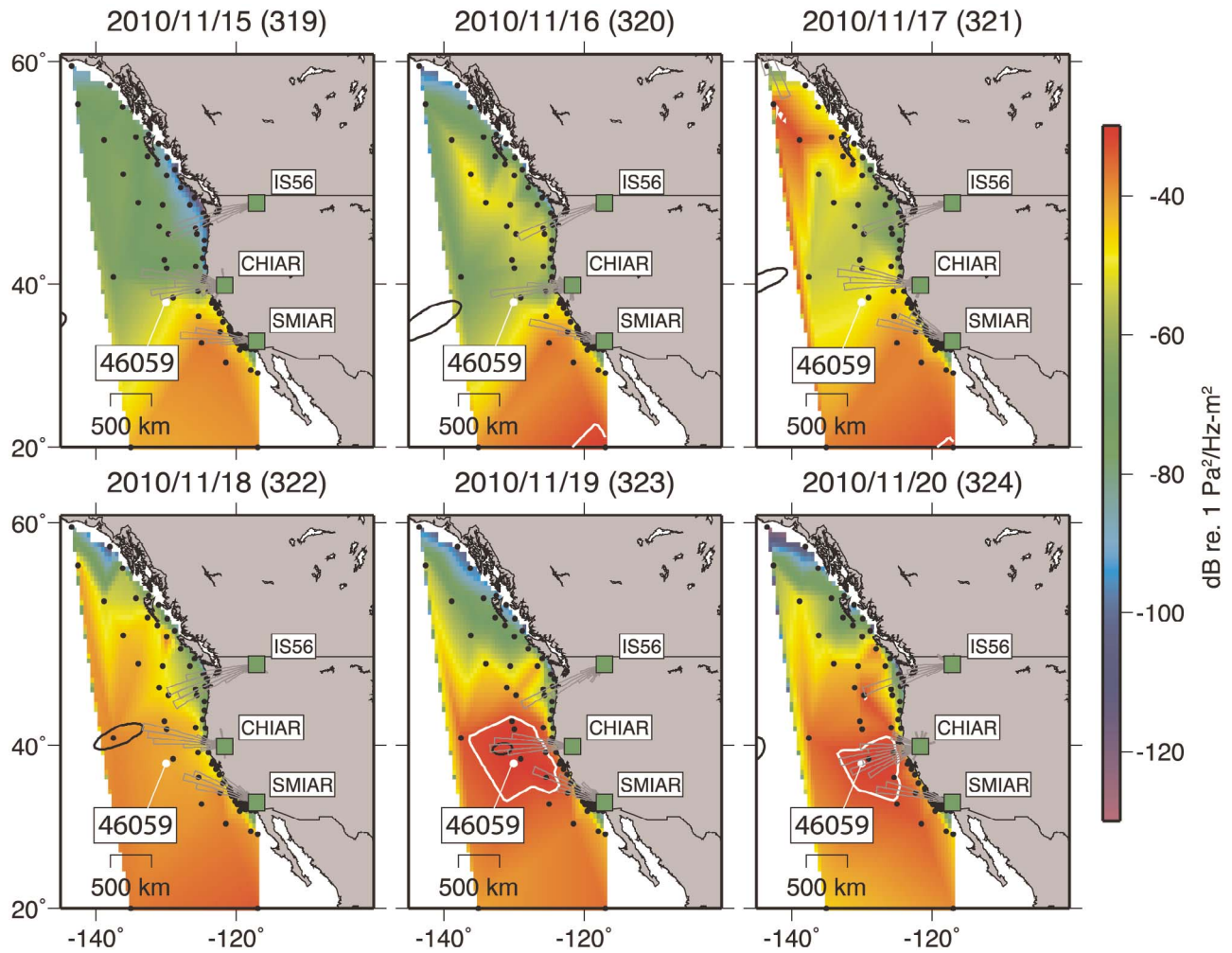


Figure 6. Prediction of $S_{MB}(x, y)$ from NWW3 model output at buoy locations compared to daily microbarom back azimuth observations shown as gray polar histograms centered at each station. A source can be seen moving from farther out in the Pacific toward the California coastline over several days. Microbaroms at IS53 in Fairbanks, Alaska, also appear to come from wave-wave interaction along the western coast of Canada on day 321.

located ~ 500 km off the northern California coast (Figures 6 and 7). On a day when observations suggest no significant microbarom energy generated at that location (15 November 2010), there are no significant sets of opposing waves of the same period. However, on day 323 when the 95% confidence region is near the buoy, there is significant opposing wave interaction at that location; a gradual shifting occurred over time, mostly of the secondary northeastward waves at 20 s periods to northwestward at 10 s periods while the direction of more prominent southeastward waves at 10 s periods remained relatively fixed. It is important to note that these two waves are propagating in directions that are parallel to the coastline, which suggests that any contribution to microbarom generation from coastal reflection was relatively insignificant during this time.

[36] The S_{MB} results above are with respect to the peak spectral values between 0.15 and 0.25 Hz. However, the microbarom source strength squared has a finite bandwidth. Figure 8 shows the computed D at buoy 46059 for the frequency span routinely output by NWW3. The peak grows

over time by about 3 orders of magnitude from a broad peak to a prominent peak at ~ 0.2 Hz on days 323 and 324. Note that there is a well-defined secondary peak on 18 November (yellow curve) between 0.3 and 0.7 Hz. It is interesting to note that this frequency range is not far from that which has been interpreted in previous studies as “surf noise” [e.g., *Arrowsmith and Hedlin, 2005*].

[37] During day 324, the two sets of waves shown in Figure 7 are still opposing at buoy 46059, and the amplitudes of the waves have not changed remarkably. However, the 95% confidence region has moved farther out to sea and the elevated levels of S_{MB} extend further northeast off the coast of Washington and southeast off the coast of Los Angeles (Figure 6). Furthermore, a prominent secondary peak in D at 0.5 Hz develops in the Los Angeles basin due to wind waves. Although all five west coast arrays were used to derive the 95% confidence region, comparing the well-defined SMIAR, CHIAR, and IS56 polar histograms with the spatial distribution of elevated S_{MB} levels suggests that the arrays are actually observing either more localized

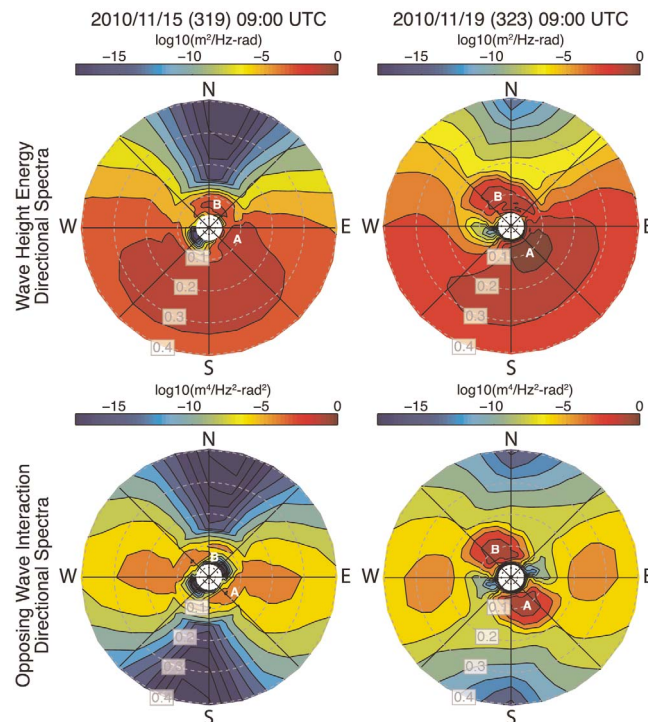


Figure 7. NWW3 estimate of directional wave spectra at buoy 46059. (top) The directional wave height energy spectra in polar coordinates with the radius equal to frequency and angle equal to the azimuth toward which the waves are traveling (oceanographic convention). (bottom) The product of the wave energy spectral values and the associated spectral values from the opposite direction. There is little opposing wave interaction on 15 November 2010. However, two well-defined sets of waves (A and B) with periods of 10 s are opposing on 19 November and predict 0.2 Hz microbarom radiation.

microbarom sources closer to the coastline or a common source outside the buoy region that is stronger in strength.

[38] The observed microbarom pressure levels during day 323 show significantly higher amplitudes detected at CHIAR than the other two arrays (Figure 9). The average difference in observed pressure levels is roughly 6 dB, which is consistent with predictions from spherical spreading from a source at buoy 46059, providing additional evidence that the 95% confidence region is well defined. On day 324 the observed amplitudes increase at CHIAR and SMIAR, but remain the same for IS56. The rise in amplitudes does not necessarily suggest that the sources observed by the arrays are closer and more localized to each array.

5. Discussion

5.1. Importance of Microbarom Source Strength

[39] It has been previously found that stratospheric winds at mid northern latitudes are the predominant factor in the detection of infrasound at the Earth's surface for frequencies below 2 Hz [Le Pichon *et al.*, 2009]. It has also been found that microbarom amplitudes in the northern hemisphere are greater during the winter than during the summer [Willis *et al.*, 2004; Le Pichon *et al.*, 2006]. The North Pacific detections in Figure 4 are interpreted as evidence that during the winter months, the microbarom sources are strong enough to be observed by most arrays (Figure 5), even those in the western Pacific in the stratospheric upwind direction. During the summer months these sources are considerably weaker, and

cannot be observed upwind by the eastern arrays. However, more efficient stratospheric propagation permits the western arrays to still detect them. Interestingly, a hybrid of these two patterns was observed by Willis *et al.* [2004] in two years of microbarom detections at IS59 (Hawaii) in the middle of the North Pacific. They found that arrivals during the fall, winter, and spring were mostly from westerly directions, similar to the pattern observed by the eastern arrays. However, IS59 detections were mostly from easterly directions during the summer, similar to the western stations. The results above therefore show that microbarom source strength is just as important as stratospheric wind strength for the detection of North Pacific microbaroms.

5.2. Resolving Pelagic Versus Coastal Sources of Microbaroms

[40] When each array detects microbaroms from a localized, coastal source, the projection of the multiple back azimuths will have some degree of intersection in the deep Pacific. The coherence in the projected back azimuths will be degraded when the detections at each array are from random directions. However, as recently shown by the inclusion of coastal reflections in NWW3 modeling, the interference of incident waves with coastal reflected waves can lead to significant sources of coastal microseisms [Ardhuin *et al.*, 2011]. If microseisms and microbaroms originate from the same source, these sources would tend to generate detections at the arrays that are not random, but point in the direction of the coastline that is closest to the

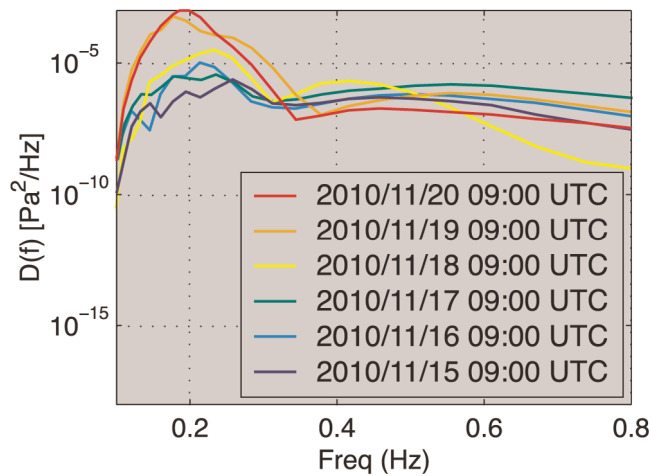


Figure 8. NWW3 prediction of microbarom source strength squared at buoy 46059. This is the evaluation of equation (7) for the same times as in Figures 6 and 7. Note the gradual increase in D by about 3 orders of magnitude over 3 days.

array, with modulations due to variations in atmospheric conditions and along-coast microbarom radiation strength. Therefore, while it is important to use a quantitative approach to locate microbarom radiation, care must be taken in the interpretation of cross-bearing location results since the common source assumption may be violated.

[41] The January 2011 microbarom detections shown in Figure 5 appear to originate from a common source that moves across the North Pacific over several days. Compared with the size of the Pacific basin, the relatively small 95% confidence region provides a measure of confidence that a single source model is appropriate for explaining the majority of observations at the arrays, especially during days 027–030.

[42] The November 2010 eastern North Pacific source of microbaroms moves eastward, over the course of 5 days, from a pelagic location ~ 2000 km off the coast until it reaches buoy 46059 on day 323 (Figure 6). During the same time, the predicted peak microbarom source strength in the area encompassing buoy 46059 grows by ~ 30 dB (Figure 8) due to the growing influence of a secondary northwestward swell that is opposing a predominant southeastward swell with the same period of 10 s (Figure 7). However, during day 324 the source location abruptly jumps ~ 1500 km offshore to an area outside the area spanned by the buoy predictions. During the same day, the predictions suggest that elevated levels of microbarom radiation near the coast continue and extend further north off the coast of Washington and south off the southern California coast. Because of the ambiguity inherent in interpreting intersecting back azimuths from a handful of arrays, it is unclear if the detections are due to a stronger source farther off the coast or to the development of more localized sources to each array near the coast. The same localization may also explain why IS59 tracks the general location of a pelagic microbarom source for 5 days before being overwhelmed by a possible localized source on day 6 (Figure 3). This interpretation is also consistent with the results of *Ardhuin et al.* [2011], who found

that on land within a few hundred kilometers of the coast, double-frequency microseisms are routinely generated by the interference of the incident and reflected waves, but that this source is routinely overpowered by a stronger source of microseisms generated in the deeper ocean between two opposing sets of waves. Nonetheless, clearly the ambiguity in locating microbarom sources with cross-bearing approaches and only a handful of arrays, especially when not compared against results of source modeling with directional wave spectra, speaks to the need for improvements in methods to locate sources of microbaroms.

5.3. Value of Directional Wave Spectra

[43] There is not a direct relationship between elevated levels of wave height and double frequency microseisms/microbaroms. Nonetheless, because spatial grids of Ψ are not part of the routine output of NWW3 models, attempts are often made to correlate significant wave height with located sources of microseisms/microbaroms. Successful correlations of microseism sources [e.g., *Gerstoft et al.*, 2008] and microbarom sources [e.g., *Landes et al.*, 2012] with elevated wave heights are often found for atmospheric depressions. Since atmospheric depressions create not only elevated wave heights, but often regions of opposing swell in the wake as demonstrated by *Stopa et al.* [2011], the elevated levels of wave height may be used to track depressions (when the ambient wavefields do not interfere) and therefore indirectly track nearby areas of opposing wave interaction. However, the boreal winter creates high seas in the Northern Hemisphere that are often not associated with well-defined depressions. In such scenarios significant wave heights do not track depressions and have limited value in studies of pelagic sources of microbaroms.

[44] Ocean waves act as a drag on the surface wind so that momentum is transferred downward, from the atmosphere into the ocean, most prominently along midlatitude storm tracks where wind speeds are generally high. Ocean waves also transfer momentum upward, creating surface winds typically in tropical latitudes where wind speeds are generally slow and swell can propagate from storms at higher latitudes [*Hanley et al.*, 2010]. It is therefore no surprise that

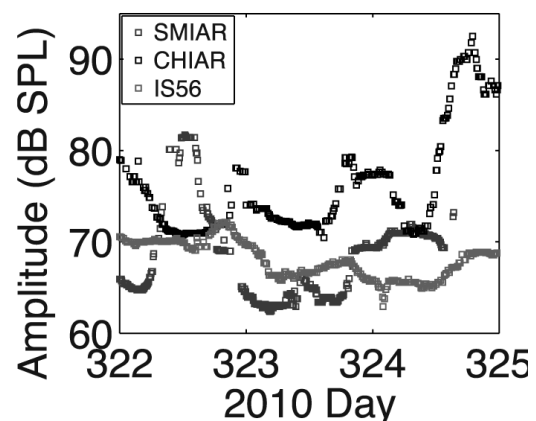


Figure 9. Observed microbarom amplitudes at west coast infrasound arrays. Shown are the microbarom detection amplitudes that have been smoothed using a 6 h long running median filter.

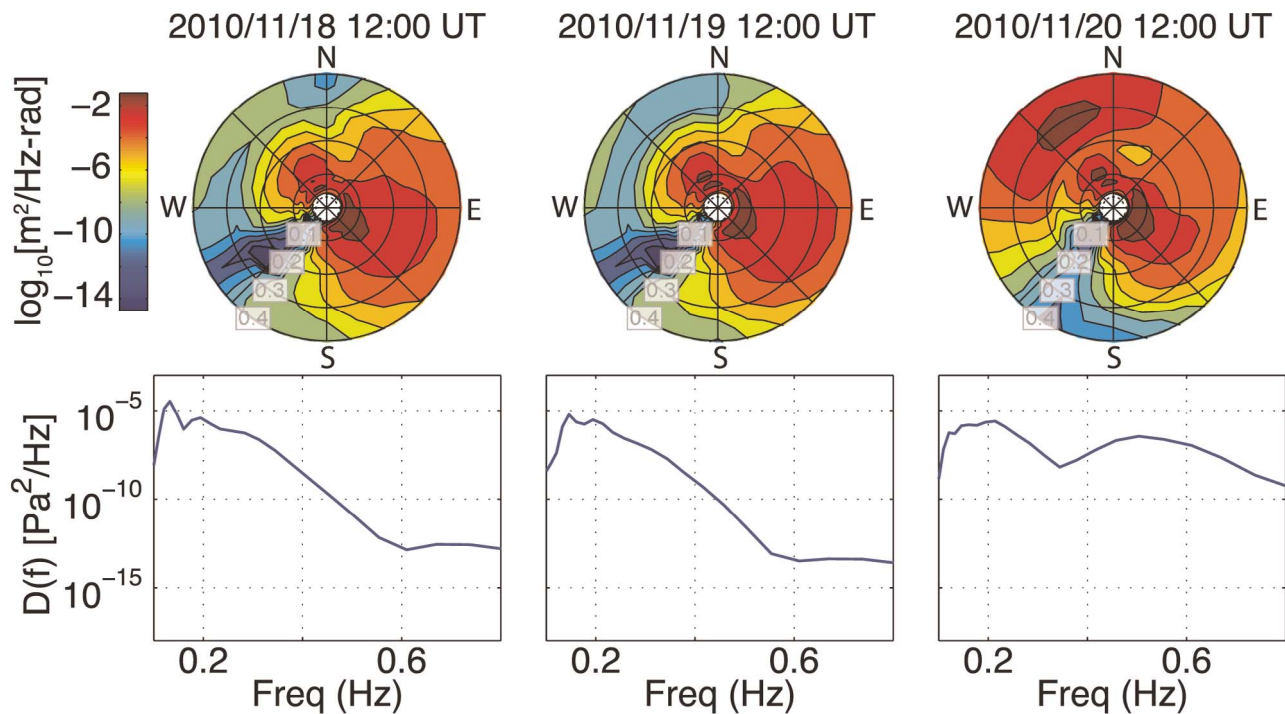


Figure 10. Directional wave energy spectra and associated microbarom source strength squared predictions during days 322–324 for buoy 46238 (Los Angeles basin) showing the growth of microbaroms due to wind waves on 20 November 2010 (day 324).

one can correlate microseism locations with areas of opposing surface winds to the south of Greenland during the turbulent boreal winter [e.g., *Kedar et al.*, 2008]. Similarly, *Hetzer et al.* [2008] found that an area of opposing dominant wave sets explained microbarom observations recorded on the island of Palau in the wake of Typhoon Usagi in the summer of 2007. In both studies, the authors show that the regions of opposing waves are clearly offset from the regions of elevated significant wave height.

[45] As shown in Figures 5 and 6, there is only, at best, a minor correlation between the observed eastern North Pacific microbarom source and the surface winds. However, the directional wave spectra from the NWW3 model output at buoy locations appear to predict well areas of opposing wave interaction in the region between pelagic and near-shore environments. Subsequent application of the *Waxler and Gilbert* [2006] model leads to predictions that generally explain the microbarom observations, even though the buoy locations are far from uniformly distributed and only extend ~ 1100 km offshore. The application of the *Longuet-Higgins* [1950] model by *Kedar et al.* [2008] to directional wave spectra output from NWW3 shows the dramatic improvement in coverage one gets by using the spectra output at all NWW3 grid points. A future NWW3 version that additionally outputs Ψ evaluated at all grid points would have a significant positive impact on future microbarom and microseism studies. Furthermore, once the WG model has been rigorously tested and perhaps expanded to include the effects of resonance, the routine NWW3 output of Ψ would facilitate the use of infrasonics as another tool to validate NWW3 model runs, especially in places with limited buoy coverage.

5.4. High-Frequency Microbaroms

[46] There have been several studies of higher-frequency (>1 Hz) infrasound that is generated or associated with ocean wave activity. *Garces et al.* [2003] and *Le Pichon et al.* [2004] showed that distinct wave breaking events along the coast can produce infrasound between 1 to 5 Hz with detectable levels at several tens of kilometers range. They found a correlation between the recorded amplitude of these signals and ocean wave heights. *Arrowsmith and Hedlin* [2005] attributed 1 to 5 Hz infrasound recorded in southern California to such “surf noise” generated along the Santa Monica coastline at a range of 100 to 400 km. They also found a correlation between the amplitude of the signals and wave height, in addition to a dependence on the stratospheric wind strength. The source mechanisms have been attributed to the collapse of barreling waves and waves crashing against rocky shorelines and exposed topographic and bathymetric features [*Garces et al.*, 2006; *Park et al.*, 2008].

[47] Microbaroms are typically thought to give rise to infrasound in the 0.1 to 0.5 Hz band. On 20 November 2010 in the Los Angeles basin, wind waves developed with a period of 3 s. These waves interacted with opposing waves to generate a secondary microbarom peak at ~ 0.5 Hz (Figure 10). This secondary peak was about 10 dB lower in strength than the 0.2 Hz microbarom peak, but this secondary peak grew 70 dB in strength over 24 h. There is also significant microbarom energy all the way up to the frequency limit of 0.8 Hz. This maximum frequency limit is twice the 0.4 Hz limit defined by NOAA in their hindcast NWW3 system. In 5 m/s winds the average wind wave period observed is

~ 1.5 s [e.g., Pierson *et al.*, 1955]. For fully developed seas under light winds (1 m/s), the Pierson-Moskowitz spectrum predicts wave periods as small as ~ 1 s [Pierson and Moskowitz, 1964]. Therefore, wind waves can give rise to infrasound with frequencies between 1 and 2 Hz. While it is clear that transient events in the surf zone create infrasound, the extension of the Waxler and Gilbert [2006] model to higher frequencies by the consideration of the shorter periods generated by routine surface winds may be another explanation for continuous sources of 0.5 to 2 Hz energy associated with ocean wave activity.

6. Conclusions

[48] The analysis of twelve infrasonic arrays located around the North Pacific rim with a time-progressive, frequency domain beamforming method illuminates North Pacific sources of pelagic and near-coastal infrasound throughout the boreal winter months that are strong enough to be observed by most arrays, even western Pacific arrays that are upwind with respect to seasonal stratospheric winds. Sources of weaker North Pacific microbarom radiation during the summer are generally only observed downwind by the western Pacific arrays. A detailed analysis of a pelagic microbarom source that is illuminated by several western U.S. arrays and moves over several days to within ~ 500 km from the eastern North Pacific coastline shows no correlation with elevated levels of significant wave height or areas of opposing dominant wave directions. At best, a minor correlation with opposing surface winds exists. However, the observed microbarom radiation is predicted well by NOAA Wave Watch 3 (NWW3) directional wave spectra output at buoy locations. Using the microbarom source physics model of Waxler and Gilbert [2006] a gradual development of two opposing, coast-parallel swells with 10 s periods ~ 500 km off the coast predicts the empirically determined source location within the resolution constraints imparted by the buoy locations.

[49] These results show that the strength of the microbarom source is just as important as that of the stratospheric winds for the detection of North Pacific microbaroms. In addition, pelagic North Pacific microbarom radiation detected by infrasonic arrays during the boreal winter could be routinely used to validate NWW3 results in regions with poor sensor coverage. Finally, this work suggests that NWW3, in its current form, can predict both pelagic sources and near-coastal microbarom sources when the opposing waves are moving parallel to the coast, which implies that it is capable of identifying a limitless supply of “ground-truthed” infrasonic sources that can be used to evaluate global detection capabilities, study source and propagation physics, and invert for models of atmospheric specifications. A future operational version of NWW3 that additionally outputs Ψ evaluated at all spatial grid points (just as significant wave height is) for several different frequencies would have a significant positive impact on future microbarom and microseism studies, even if coastlines remain absorbing boundaries that exclude using NWW3 for modeling microbarom/microseism generation due to coastal reflection of broadside waves.

[50] **Acknowledgments.** This paper is dedicated to Brendon Armstrong (1987–2011), whose creativity, dedication, and hard work in the installation

and maintenance of the Chico infrasonic array (CHIAR) were critical to the success of this project. J. Mott, J. Rowden, P. Maslin, B. Gallaway, S. Huber, and the other volunteers of the California State University’s Big Chico Creek Ecological Reserve provided invaluable assistance with installing, maintaining, and disassembling CHIAR. P. Bryant, C. Coon, J. Chang, D. Chavez, M. Davis, S. DeWolf, M. Hedlin, D. Horwitt, M. Kirk, J. Lyons, M. Rahn, R. Shelby, J. White, H. Wuhmann, F. Wyatt, and M. Zumberge assisted in the development and deployment of CHIAR and the Santa Margarita infrasonic array (SMIAR). R. Shelby created Web tools that facilitated this work. C. Szuberla and K. Dawson provided IS53 data. M. Garces provided the microbarom detections for IS59 shown in Figure 3. NVIAR array data were provided by P. Golden. D. Drob provided assistance with managing the ground-to-space atmospheric velocity modeling system mirror at UCSD. Discussions with M. Zumberge, R. Waxler, L. Romero, M. Garces, P. Gerstoft, and R. Rembold assisted this work. Two anonymous reviewers provided constructive comments that improved this paper. This work was funded by NOAA under award 09-09-023 (University of Mississippi).

References

- Ardhuin, F., E. Stutzmann, M. Schimmel, and A. Mangeney (2011), Ocean wave sources of seismic noise, *J. Geophys. Res.*, *116*, C09004, doi:10.1029/2011JC006952.
- Arrowsmith, S., and M. A. H. Hedlin (2005), Observations of infrasound from surf in Southern California, *Geophys. Res. Lett.*, *32*, L09810, doi:10.1029/2005GL022761.
- Baird, H. F., and C. J. Banwell (1940), Recording of air pressure oscillations associated with microseisms at Christchurch, *N. Z. J. Sci. Technol., Sect. B*, *21*, 314–329.
- Benioff, H., and B. Gutenberg (1939), Waves and currents recorded by electromagnetic barographs, *Bull. Am. Meteorol. Soc.*, *20*, 421–426.
- Bernard, P. (1937), Relation entre la houle sur la Cote du Maroc et l’oritation microseismique en Europe occidentale, *C. R. Acad. Sci. Paris*, *205*, 163–166.
- Brekhovskikh, I. M., V. V. Goncharov, V. M. Kurtepov, and K. A. Naugolnykh (1973), The radiation of infrasound into the atmosphere by surface waves in the ocean, *Atmos. Ocean. Phys.*, *9*, 899–907.
- Bromirski, P. D. (2001), Vibrations from the “Perfect Storm,” *Geochem. Geophys. Geosyst.*, *2*(7), 1030, doi:10.1029/2000GC000119.
- Bromirski, P. D., F. K. Duennebier, and R. A. Stephen (2005), Mid-ocean microseisms, *Geochem. Geophys. Geosyst.*, *6*, Q04009, doi:10.1029/2004GC000768.
- Cansi, Y. (1995), An automated seismic event processing for detection and location: The P.M.C.C. method, *Geophys. Res. Lett.*, *22*, 1021–1024, doi:10.1029/95GL00468.
- Cessaro, R. K. (1994), Sources of primary and secondary microseisms, *Bull. Seismol. Soc. Am.*, *84*, 142–148.
- Christie, D. R., and P. Campus (2010), The IMS infrasound network: Design and establishment of infrasound stations, in *Infrasound Monitoring for Atmospheric Studies*, edited by A. Le Pichon, E. Blanc, and A. Hauchecorne, pp. 29–75, Springer, New York, doi:10.1007/978-1-4020-9508-5_2.
- Darbyshire, J. (1962), Microseisms, in *The Sea*, vol. 1, pp. 700–719, John Wiley, London.
- Deacon, G. E. R. (1947), Relation between sea-waves and microseisms, *Nature*, *162*, 419–421.
- DeMuth, G. L. (1977), Frequency domain beamforming techniques, in *Acoustics, Speech, and Signal Processing, IEEE International Conference on ICASSP ’77*, pp. 713–715, IEEE Press, Piscataway, N. J., doi:10.1109/ICASSP.1977.1170316.
- Donn, W. L., and B. Naini (1973), Sea wave origin of microbaroms and microseisms, *J. Geophys. Res.*, *78*, 4482–4488, doi:10.1029/JC078i021p04482.
- Donn, W. L., and E. S. Posmentier (1967), Infrasonic waves from the marine storm of April 7, 1966, *J. Geophys. Res.*, *72*, 2058–2061.
- Donn, W. L., and D. Rind (1971), Natural infrasound as an atmospheric probe, *Geophys. J. R. Astron. Soc.*, *26*, 111–133.
- Drob, D. P., R. R. Meier, J. M. Picone, and M. Garces (2010a), Inversion of infrasound signals for passive atmospheric remote sensing, in *Infrasound Monitoring for Atmospheric Studies*, edited by A. Le Pichon, E. Blanc, and A. Hauchecorne, pp. 701–732, Springer, Dordrecht, Netherlands.
- Drob, D. P., M. M. Garces, M. A. H. Hedlin, and N. Brachet (2010b), The temporal morphology of infrasound propagation, *Pure Appl. Geophys.*, *167*, 437–453, doi:10.1007/s00024-010-0080-6.
- Friedrich, A., F. Kruger, and K. Klinge (1998), Ocean-generated microseismic noise located with the Grafenberg array, *J. Seismol.*, *2*, 47–64.
- Frigo, M., and S. Johnson (1999), A fast Fourier transform compiler, in *Proceedings of ACM SIGPLAN ’99 Conference Programming Language Design and Implementation (PLDI)*, vol. 34, pp. 169–180, Assoc. for Comput. Mach., New York.

- Garces, M., C. Hetzer, M. Merrifield, M. Willis, and J. Aucan (2003), Observations of surf infrasound in Hawai'i, *Geophys. Res. Lett.*, *30*(24), 2264, doi:10.1029/2003GL018614.
- Garces, M., M. Willis, C. Hetzer, A. Le Pichon, and D. Drob (2004), On using ocean swells for continuous infrasonic measurement of winds and temperature in the lower, middle, and upper atmosphere, *Geophys. Res. Lett.*, *31*, L19304, doi:10.1029/2004GL020696.
- Garces, M., J. Aucan, D. Fee, P. Caron, M. Merrifield, R. Gibson, J. Bhattacharyya, and S. Shah (2006), Infrasound from large surf, *Geophys. Res. Lett.*, *33*, L05611, doi:10.1029/2005GL025085.
- Gerstoft, P., and T. Tanimoto (2007), A year of microseisms in southern California, *Geophys. Res. Lett.*, *34*, L20304, doi:10.1029/2007GL031091.
- Gerstoft, P., M. C. Fehler, and K. G. Sabra (2006), When Katrina hit California, *Geophys. Res. Lett.*, *33*, L17308, doi:10.1029/2006GL027270.
- Gerstoft, P., P. M. Shearer, N. Harmon, and J. Zhang (2008), Global P, PP, and PKP wave microseisms observed from distant storms, *Geophys. Res. Lett.*, *35*, L23306, doi:10.1029/2008GL036111.
- Gilmore, M. H. (1946), Microseisms and ocean storms, *Bull. Seismol. Soc. Am.*, *36*, 89–119.
- Gutenberg, B., and H. Benioff (1941), Atmospheric-pressure waves near Pasadena, *Eos Trans. AGU*, *22*, 424–426.
- Hanley, K. E., S. E. Belcher, and P. P. Sullivan (2010), A global climatology of wind-wave interaction, *J. Phys. Oceanogr.*, *40*, 1263–1282.
- Haubrich, R. A., and K. McCamy (1969), Microseisms: Coastal and pelagic sources, *Rev. Geophys.*, *7*, 539–571.
- Haubrich, R. A., W. H. Munk, and F. E. Snodgrass (1963), Comparative spectra on microseisms and swell, *Bull. Seismol. Soc. Am.*, *53*, 27–37.
- Hasselmann, K. (1963), A statistical analysis of the generation of microseisms, *Rev. Geophys. Space Phys.*, *1*, 177–210.
- Hedlin, M. A. H., K. Walker, D. Drob, and C. D. de Groot-Hedlin (2012), Infrasound: Connecting the solid Earth, oceans and atmosphere, *Annu. Rev. Earth Planet. Sci.*, *40*, 327–354, doi:10.1146/annurev-earth-042711-105508.
- Hetzer, C. H., R. Waxler, K. E. Gilbert, C. L. Talmadge, and H. E. Bass (2008), Infrasound from hurricanes: Dependence on the ambient ocean surface wave field, *Geophys. Res. Lett.*, *35*, L14609, doi:10.1029/2008GL034614.
- Iyer, H. M. (1958), A study of direction of arrival of microseisms at Kew Observatory, *Geophys. J. Int.*, *1*, 32–43.
- Jenkins, G. M., and D. G. Watts (1968), *Spectral Analysis and Its Applications*, Holden-Day, San Francisco, Calif.
- Kedar, S., M. Longuet-Higgins, F. Webb, N. Graham, R. Clayton, and C. Jones (2008), The origin of deep ocean microseisms in the North Atlantic Ocean, *Proc. R. Soc., Ser. A*, *464*, 777–793, doi:10.1098/rspa.2007.0277.
- Kulichkov, S. N., K. V. Avilov, O. E. Popov, A. I. Otrezov, G. A. Bush, and A. K. Baryshnikov (2004), Some results of simulation of long-range infrasonic propagation in the atmosphere, *Izv. Atmos. Ocean. Phys.*, *40*, 202–215.
- Landes, M., L. Ceranna, A. Le Pichon, and R. S. Matoza (2012), Localization of microbarom sources using the IMS infrasound network, *J. Geophys. Res.*, *117*, D06102, doi:10.1029/2011JD016684.
- Le Pichon, A., V. Maurer, D. Raymond, and O. Hyvernaud (2004), Infrasound from ocean waves observed in Tahiti, *Geophys. Res. Lett.*, *31*, L19103, doi:10.1029/2004GL020676.
- Le Pichon, A., E. Blanc, and D. Drob (2005), Probing high-altitude winds using infrasound, *J. Geophys. Res.*, *110*, D20104, doi:10.1029/2005JD006020.
- Le Pichon, A., L. Ceranna, M. Garces, D. Drob, and C. Millet (2006), On using infrasound from interacting ocean swells for global continuous measurements of winds and temperature in the stratosphere, *J. Geophys. Res.*, *111*, D11106, doi:10.1029/2005JD006690.
- Le Pichon, A., J. Vergoz, E. Blanc, J. Guilbert, L. Ceranna, L. Evers, and N. Brachet (2009), Assessing the performance of the International Monitoring System's infrasound network: Geographical coverage and temporal variabilities, *J. Geophys. Res.*, *114*, D08112, doi:10.1029/2008JD010907.
- Longuet-Higgins, M. S. (1950), A theory of the origin of microseisms, *Philos. Trans. R. Soc., Ser. A*, *243*, 1–35.
- Miche, M. (1944), Mouvements ondulatoires de la mer en profondeur constant ou décroissante, *Ann. Ponts Chaussees*, *114*, 25–87, 131–164, 270–292, 396–406.
- Park, J., M. Garces, D. Fee, and G. Pawlak (2008), Collective bubble oscillations as a component of surf infrasound, *J. Acoust. Soc. Am.*, *123*, 2506–2512, doi:10.1121/1.2885743.
- Pierson, W. J., Jr., and L. A. Moskowitz (1964), Proposed spectral form for fully developed wind seas based on the similarity theory of S. A. Kitaigorodskii, *J. Geophys. Res.*, *69*, 5181–5190.
- Pierson, W. J., Jr., G. Neumann, and R. W. James (1955), *Practical Methods for Observing and Forecasting Waves by Means of Wave Spectra and Statistics*, Publ. No. 603, Hydrogr. Off., U.S. Navy Dep., Washington, D. C.
- Ramirez, J. E. (1940), An experimental investigation of the nature and origin of microseisms at St. Louis, Mo., *Bull. Seismol. Soc. Am.*, *30*, 35–84, 139–178.
- Rind, D., and W. L. Donn (1975), Further use of natural infrasound as a continuous monitor of the upper atmosphere, *J. Atmos. Sci.*, *32*, 1694–1704.
- Silver, P. G., and W. W. Chan (1991), Shear wave splitting and subcontinental mantle deformation, *J. Geophys. Res.*, *96*, 16,429–16,454.
- Stopa, J. E., K. F. Cheung, M. A. Garces, and D. Fee (2011), Source of microbaroms from tropical cyclone waves, *Geophys. Res. Lett.*, *38*, L05602, doi:10.1029/2010GL046390.
- Tabulevich, V. N. (1995), On recordings of global microseismic vibrations and observations of microseisms in shore zones of oceans, *Phys. Earth Planet. Inter.*, *91*, 299–305.
- Walker, K. T., and M. A. H. Hedlin (2010), A review of wind noise reduction methodologies, in *Infrasound Monitoring for Atmospheric Studies*, edited by A. Le Pichon, E. Blanc, and A. Hauchecorne, pp. 141–182, Springer, New York, doi:10.1007/978-1-4020-9508-5.
- Walker, K. T., R. Shelby, M. A. H. Hedlin, C. D. de Groot-Hedlin, and F. Vernon (2011), Western U.S. infrasonic catalog: Illuminating infrasonic hot spots with the USArray, *J. Geophys. Res.*, *116*, B12305, doi:10.1029/2011JB008579.
- Waxler, R., and K. E. Gilbert (2006), The radiation of atmospheric microbaroms by ocean waves, *J. Acoust. Soc. Am.*, *119*, 2651–2664.
- Wiechert, E. (1904), Verhandlugen der zweiten Internationalen Seismologischen Konferenz, *Gerlands Beitr. Geophys.*, *2*, 41–43.
- Willis, M., M. Garces, C. Hetzer, and S. Businger (2004), Infrasonic observations of open ocean swells in the Pacific: Deciphering the song of the sea, *Geophys. Res. Lett.*, *31*, L19303, doi:10.1029/2004GL020684.
- Zhang, J., P. Gerstoft, and P. D. Bromirski (2010), Pelagic and coastal sources of P-wave microseisms: Generation under tropical cyclones, *Geophys. Res. Lett.*, *37*, L15301, doi:10.1029/2010GL044288.
- Zumberge, M. A., J. Berger, M. A. H. Hedlin, E. Husmann, S. Nooner, R. Hilt, and R. Widmer-Schmidrig (2003), An optical fiber infrasound sensor: A new lower limit on atmospheric pressure noise between 1 and 10 Hz, *J. Acoust. Soc. Am.*, *113*, 2474–2479.